

Wiley Journal of Nanotechnology Volume 2025, Article ID 6674176, 16 pages https://doi.org/10.1155/jnt/6674176



# Research Article

# Aloe Vera-Assisted Synthesis of Dy-Doped MgNb<sub>2</sub>O<sub>6</sub> for Sustainable Sensing and Photocatalytic Applications

N. Basavaraju, H. N. Shwetha, C. R. Ravikumar, Syed Khasim, K. B. Tan, Kiflom Gebremedhn Kelele, K. Y. Chan, and H. C. Ananda Murthy, Ananda Murthy,

Correspondence should be addressed to C. R. Ravikumar; ravicr128@gmail.com and H. C. Ananda Murthy; anandkps350@gmail.com

Received 19 November 2024; Accepted 5 April 2025

Academic Editor: Mozhgan Afshari

Copyright © 2025 N. Basavaraju et al. Journal of Nanotechnology published by John Wiley & Sons Ltd. This is an open access article under the terms of the Creative Commons Attribution License, which permits use, distribution and reproduction in any medium, provided the original work is properly cited.

This study introduces a novel, cost-effective, and combustion synthesis approach for synthesizing dysprosium-doped magnesium niobium oxide (Dy: MNbO) nanoparticles (NPs) via a solution combustion method utilizing aloe vera gel as a green fuel. The use of aloe vera gel not only simplifies the synthesis process but also enhances the ecocompatibility of the method, making it a significant advancement over conventional techniques. Advanced spectral techniques were employed to characterize the Dy: MNbO NPs. PXRD analysis revealed that the average crystalline size of the NPs was approximately 45 nm. The energy band gap of the synthesized Dy: MNbO NPs was determined to be in the range of 4-5 eV. SEM analysis showed the presence of distinctly agglomerated, lump-like structures. The photocatalytic performance of Dy: MNbO NPs was evaluated for the degradation of industrial dyes, specifically direct green (DG) dye, under UV light irradiation. Among different doping concentrations, the 4 mol% Dy: MNbO NPs exhibited the highest photocatalytic efficiency, achieving an 82% degradation. In comparison, the degradation rates for other doping concentrations were 58% for 2 mol%, 62% for 6 mol%, and 75% for 8 mol%. Electrochemical analyses using 4 mol% Dy: MNbO NPs as a modified electrode were performed in a 0.1 M HCl electrolyte solution. Cyclic voltammetry (CV) and electrochemical impedance spectroscopy (EIS) confirmed the reversibility of the electrode reaction. The sample demonstrated excellent performance in electrochemical sensing applications, specifically for detecting ibuprofen and glucose molecules.

Keywords: direct green; dysprosium; electrochemical sensor; glucose; ibuprofen; magnesium niobium oxide

# 1. Introduction

The multifunctional properties of metal oxide nanoparticles (NPs) make them highly relevant for water purification technologies, offering cost-effective and environmentally

friendly solutions to address the growing global water crisis. Their application in water treatment, such as pollutant degradation, microbial disinfection and heavy metal removal, aligns with the urgent need for clean water [1–6]. The textile dyeing industries are major contributors to water

<sup>&</sup>lt;sup>1</sup>Department of Basic Science, East West Institute of Technology, Bangalore 91, Karnataka, India

<sup>&</sup>lt;sup>2</sup>Department of Mathematics, BGSIT, Adichunchanagiri University BG-Nagar, Belur, Karnataka, India

<sup>&</sup>lt;sup>3</sup>Department of Physics, Faculty of Science, University of Tabuk, Tabuk 71491, Saudi Arabia

<sup>&</sup>lt;sup>4</sup>Department of Chemistry, Faculty of Science, Universiti Putra Malaysia, UPM, Serdang 43400, Selangor, Malaysia

<sup>&</sup>lt;sup>5</sup>Department of Chemistry, College of Natural and Computational Science, Woldia University, Woldia, Ethiopia

<sup>&</sup>lt;sup>6</sup>Centre for Advanced Devices and Systems, Faculty of Artificial Intelligence and Engineering, Multimedia University, Persiaran Multimedia, Cyberjaya 63100, Selangor, Malaysia

<sup>&</sup>lt;sup>7</sup>School of Applied Sciences, Papua New Guinea University of Technology, Lae 411, Morobe, Papua New Guinea

<sup>&</sup>lt;sup>8</sup>Department of Prosthodontics, Saveetha Dental College & Hospital,

Saveetha Institute of Medical and Technical Science (SIMATS), Saveetha University, Chennai 600077, Tamil Nadu, India

pollution, producing large volumes of contaminated wastewater that affect global water streams [7]. To address this critical issue, various strategies have been implemented, to treat the contaminated water, which are membrane filtration [8], bioadsorption [9], ion exchange [10], biological and aerobic treatments [11], coagulation [12], and ozonation [13]. Among these methods, ion exchange has been widely used to remove contaminants such as heavy metals and nitrates from wastewater. However, it has several limitations: (1) high selectivity: While effective for specific ions, it is less efficient for removing organic compounds; (2) resin regeneration: Periodic regeneration of the resin generates secondary waste, which poses additional disposal challenges; (3) cost: Frequent resin replacement and regeneration significantly increase operational costs. Photocatalytic degradation has emerged as an advanced and sustainable alternative for wastewater treatment. This method is highly effective in breaking down a wide range of organic and inorganic pollutants. It is economically viable and easy to operate and does not generate secondary waste, making it an attractive solution for environmental remediation [14, 15].

2

The rare earth oxides (e.g., La, Ce, Dy) are widely recognized as excellent catalysts due to their ability to alternate between oxidation states, and in electrochemical study their enhancing fuel cell efficiency, and their effectiveness as additives in solid electrolytes [16, 17]. In this study, dysprosium (Dy) was selected for its unique electronic configuration and its ability to enhance the structural, optical, functional properties of oxide NPs. Dy: MgNb2O6 exhibits a columbite-type orthorhombic structure, classified under the Pbcn space group with interconnected [MgO<sub>6</sub>] and [NbO<sub>6</sub>] octahedral units. The particle size varies depending on the synthesis method, typically ranging from 20 to 50 nm in combustion synthesis [18–20]. The incorporation of  $Dy^3$ + into the MgNb2O6 lattice introduces slight distortions due to the size mismatch between Dy<sup>3+</sup> and Mg<sup>2</sup> ions. It leads to unique electronic transitions of Dy ions, which enhance the optical absorption spectrum, thereby increasing the photocatalytic efficiency of MgNb<sub>2</sub>O<sub>6</sub>, particularly under visible light. Additionally, the incorporation of Dy is expected to introduce localized energy states, reduce the recombination rate of charge carriers and further improve the photocatalytic activity. Dy: MNbO NPs demonstrates improved electron mobility and enhanced reversibility in electrochemical reactions, making it particularly effective for sensing applications [21].

Conventional physical and chemical methods for synthesizing rare earth-doped metal oxide NPs such as sol-gel processes [22], coprecipitation [23], hydrothermal techniques [24], wet chemical methods [25] and solid state synthesis [26] are often costly and time-intensive. In contrast, combustion synthesis emerges as a highly efficient, cost-effective and rapid alternative for synthesizing the rare earth-doped metal oxide NPs. This exothermic method generates high reaction temperatures, promoting rapid crystallization of materials and significantly reducing synthesis time, making it a promising approach for synthesis of NPs used in wide range of applications [27, 28].

In the synthesis of rare earth-doped metal oxides, green fuels act as reducing agents and structure-directing templates, influencing particle morphology, size and crystallinity. The presence of natural compounds like polysaccharides, flavonoids and proteins in green fuels helps regulate nucleation and growth, leading to improved functional properties such as enhanced photocatalytic efficiency, superior electrochemical performance and better thermal stability [29, 30]. Aloe vera (AV) gel was chosen as a green fuel due to its nontoxicity, affordability, safety and biodegradability. AV gel plays a crucial role in controlling NP morphology, influencing their size and shape [31]. This effect is attributed to the presence of polysaccharides, which modify surface energy and promote uniform growth. As a green fuel, AV gel offers a sustainable and environmentally friendly approach to NP synthesis [32].

This study focuses on the synthesis of Dy: MNbO NPs via a combustion method utilizing AV gel as a fuel. The use of environmentally benign fuels in combustion synthesis not only reduces toxic by-products but also improves the structural integrity and electrochemical performance of the synthesized materials. These enhanced properties, including high surface area, superior conductivity and improved electrocatalytic activity, make them highly suitable for advanced electrochemical sensing applications. In particular, their effectiveness in detecting ibuprofen and glucose molecules highlights their potential for use in biomedical and environmental monitoring.

# 2. Materials and Methods

2.1. Preparation of NP. The green combustion method is used to prepare the 2 mol% of Dy: MNbO NPs. The stoichiometric amounts of niobium pentoxide (Nb<sub>2</sub>O<sub>5</sub>) of 0.079 g, magnesium nitrate (Mg(NO<sub>3</sub>)<sub>2</sub> of 4.31 g, dysprosium nitrate (Dy(NO<sub>3</sub>)<sub>3</sub> of 0.313 g (2%, 4%, 6% and 8%), ammonium nitrate (NH<sub>4</sub>(No<sub>3</sub>)<sub>2</sub> of 0.21 g were brought from Sigma-Aldrich, and 5 mL of AV gel is used as fuel. The crude AV leaves were collected in the early morning as production of gel is highest at that time. And we selected mature and healthy leaves from the outer section of the AV plant. The scalp of AV leaf was removed and the leaves were washed thoroughly with distilled water. The extracted gel was blended into a liquid using a blender to ensure uniformity. The liquid was filtered through fine mesh to remove any solid residues and was stored in freezer maintained at 4°C until use. And, 5% of AV gel is used as a fuel and AV gel functions as both a reducing agent and gelling agent, while the nitrates in the precursor act as oxidizing agents. Initially, stoichiometric amounts of niobium pentoxide (Nb<sub>2</sub>O<sub>5</sub>), magnesium nitrate (Mg(NO<sub>3</sub>)<sub>2</sub>, ammonium nitrate  $(NH4(No_3)_2, dysprosium nitrate (Dy(NO_3))_3 were taken in$ Petri dish and the double-distilled water was added and it is stirred for 20 minutes and 5 mL AV gel was added. And it was finally transferred to silica crucible and then placed in a preheated muffle furnace of maintaining temperature  $750 \pm 10^{\circ}$ C; at this temperature, decomposition of chemical precursors begins and AV gel produces high-energy

conditions for NP formation, which initiates nucleation and early stages of NP growth.

After the chemical mixture is started to boil, water is vaporized and mixture catches the fire, and finally, white powder is obtained. The obtained powder is calcined at 1000°C for 3 h, which also helps in controlling the particle size as shown in Figure 1. Higher temperatures drive the particles to grow larger, improving the crystallinity and reducing defects. This temperature ensures that the particles reach a stable size and morphology while minimizing the formation of amorphous regions that could affect the properties of the NPs.

2.2. Photocatalytic Analysis. The photodegradation of DG dye ( $C3_4H_{23}N_7Na_2O_8S_2$ ) of its maximum absorption peak at 625 nm recorded under UV light irradiation. In the experimental technique, 20 ppm of direct green (DG) dye solution was taken in a circular dish and 20 mg of catalyst (Dy: MNbO) was added. The mixture is exposed to UV light irradiation using a 400-W mercury lamp and stirred with a magnetic stirrer. Every 15 min, 5 mL of dye solution is pipetted out of the dish. This process was continued for 120 min. The pipetted solution was then centrifuged and subjected to UV-vis spectrometry testing, which produces absorbance spectra [19].

2.3. Preparation of the Graphite Dy: MNbO NP Electrode for Electrochemical and Sensing Studies. To prepare the working electrode with 4 mol% Dy: MNbO (NPs), the Dy: MNbO NPs were mixed with graphite powder and silicon oil (density: 0.98–1.0 g/mL at 20°C, viscosity: 370–500 mPas) in a ratio of 15:70:15. The mixture was ground thoroughly in a mortar for 25 min to ensure uniform blending. The prepared paste was then packed into a tube containing a copper wire with a diameter of 0.3 mm to serve as the electrode contact. The modified Dy: MNbO NP electrode was tested in a 0.1 M HCl (Sigma Aldrich) aqueous electrolyte solution. This electrode was utilized for sensing ibuprofen in the concentration range of 1–5 mM and for glucose sensing, demonstrating the applicability of 4 mol% Dy: MNbO NPs in electrochemical sensing [33].

2.4. Instruments. The phase purity of the compounds was analysed by powder X-ray diffraction (XRD). The instrument operated at 50 kV and 20 mA, utilizing CuKα radiation with a wavelength of 1.541 Å. A nickel filter was employed, and the scan rate was set at  $20 \,\mathrm{min}^{-1}$ . The surface morphology of the NP was examined in scanning electron microscope (SEM) for high-resolution image of surface of the material. Transmission electron microscopy (TEM) measurements were carried out using a JEOL JEM-2100 instrument. The accelerating voltage was capable of reaching up to 200 kV, and a LaB6 filament was employed. Diffuse reflectance spectra (DRS) were recorded by Perkin-Elmer UV-vis spectrometer. Fourier-transform infrared spectroscopy (FTIR) was utilized to identify the functional groups and chemical bonds present in the prepared sample,

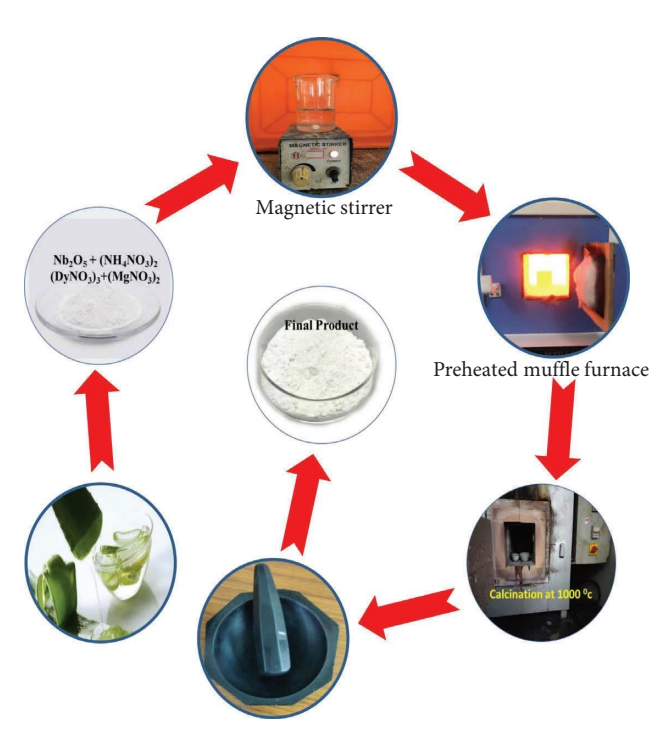


FIGURE 1: Schematic representation of the steps involved in the combustion process.

providing insights into its molecular composition. The UV-vis absorption spectra were analysed using a Shimadzu UV-vis, uv-26000 instrument. The measurements were conducted within the range of 200–800 nm. The electrochemical investigations of the prepared nanomaterials were conducted utilizing a CHI608E potentiostat in three-electrode system consisting of a nanomaterial coated with carbon paste electrode, a platinum wire and an Ag/AgCl electrode, which were employed as the working, counter and reference electrodes in 0.1 M HCl solutions at various scan rates, respectively.

#### 3. Results and Discussions

XRD plays a vital role in determining the crystal structure and phase of the synthesized NPs. Figure 2(a) shows the XRD patterns of the green combustion synthesized Dy: MNbO (2-8 mol%) NPs, confirming the effective synthesis due to incorporation of the Dy<sup>3+</sup> ions into the host material, which did not disrupt the crystal structure, and no additional peaks were obtained by the incorporation of Dy<sup>3+</sup> ions. Interestingly, all the detected diffraction peaks exactly match the standard JCPDS No. 33-0875 [34]. The observed XRD peaks reveal the crystalline form, and the peak position verifies the columbite-type orthorhombic structure, belonging to the Pbcn space group and D2h point group symmetry [35]. Additionally, Scherer's approach was utilized to determine the typical particle size (D) using Equation 1, and the particle size is in 20-50 nm range and also strain was calculated (Table 1) [36]. The major significance of dopant is the rises in the dopant concentration, and the primary diffraction peaks shift towards lower angle side, resulting in the decreased intensity as revealed in the XRD

pattern shown in Figure 2(b). The presence of Dy<sup>3+</sup> ions in the host matrix leads to tensile stress and microstrain decreases, and the estimated crystalline size increases with dopant concentration (Table 1), causing PXRD peaks to shift in the direction of the lower angle side.

$$D = \frac{0.9\lambda}{\beta \cos \theta},$$

$$\varepsilon = \frac{\beta \cos \theta}{4},$$

$$D_x = \frac{16M}{Na^3},$$
(1)

$$SF = \left[ \frac{2\pi^2}{45\sqrt{3}\tan\theta} \right],$$

$$V = a^3, (2)$$

$$\delta = \frac{1}{D^2},\tag{3}$$

where D: crystallite size (in nanometres, nm),  $\lambda$ : wavelength of the X-ray,  $\beta$ : full width at half maximum (FWHM) of the diffraction peak and  $\theta$ : Bragg's angle;  $\varepsilon$ : microstrain, density ( $D_{\star}$ ), dislocation density ( $\delta$ ) and stacking fault (SF).

Figure 3 shows the FTIR spectra of green combustion synthesized Dy: MNbO (2-8 mol%) NPs measured at rate of (400-4000 cm<sup>-1</sup>). The FTIR detects functional groups in organic and inorganic substances based on the various vibrational frequencies and is crucial for detecting the chemical composition of the NPs. The transmittance peaks at 3446 cm<sup>-1</sup> is attributed due to vibrations in hydroxyl (OH) groups; that is, H-O-H indicates the presence of O-H hydroxyl stretch. This stretch is characteristic of water. 2924 cm<sup>-1</sup> is formed due to the asymmetric stretching vibration of CH groups methylene (CH<sub>2</sub>) or methyl (CH<sub>3</sub>) groups C-H stretch from alkyl groups, 2360 cm<sup>-1</sup> is the presence of a gas-phase carbon dioxide (CO<sub>2</sub>) alkyne stretch for a C≡C triple bond such as in alkynes, 1644 cm<sup>-1</sup> is associated with the stretching vibration of the double bond (C=C) group stretch in alkenes and aromatic rings, and 1498 cm<sup>-1</sup> is formed due to vibrations associated with the aromatic C-H bending in aromatic compounds. A peak at 1083 cm<sup>-1</sup> in an FTIR spectrum C-O stretch: This is the most common interpretation, especially for ethers and alcohols; 853 cm<sup>-1</sup> is formed due to C-H out-of-plane bending in aromatic compounds, particularly orthosubstituted benzene rings. And 565 cm<sup>-1</sup> is formed due to metal-oxygen stretching and bending vibrations in Mg-O or Nb-O (octahedral metaloxygen) [37, 38].

The DRS technique was used to record the optical properties of the produced Dy: MNbO NPs, with measurements taken from 200 to 800 nm, as shown in Figure 4(a). Using the Kubelka–Munk method (Equation (4)), the diffuse reflectance data of Dy: MNbO NPs were converted into an absorption coefficient ( $\alpha$ ). In this method, the reflectance is inversely proportional to the scattering

coefficient (S) and directly related to the absorption coefficient (K) [39].

$$F(R) = \frac{(1-R)^2}{2R} = \frac{K}{S}.$$
 (4)

The Tauc equations (Equation (5)) of linear absorption coefficient ( $\alpha$ ) are used to determine the energy band gap (Eg) of prepared Dy: MNbO NPs, where 'n' determines the transition of the prepared sample where n = 1 denotes direct transition and n = 1/2 indirect transition; we are using indirect transition to find band gap.

$$\alpha = \frac{C_1 \left(hv - Eg\right)^n}{hv},\tag{5}$$

where  $\alpha$ : absorption coefficient.  $C_1$ : is constant,  $h\nu$ : energy of the incident photon, where h: Planck's constant,  $\nu$ : frequency of the photon (in Hz), Eg: band gap energy of the material (in eV) and n: power exponent that depends on the type of electronic transition.

The band gap of the prepared Dy: MNbO NPs was determined by drawing a tangent to the linear portion of the  $(F(R)h\nu)^2$  versus  $h\nu$  plot, as shown in Figure 4(b) [40, 41]. The calculated band gap values ranged from 4.85 to 5.01 eV. The band gap of the doped sample decreased with increasing doping concentration. This reduction can be attributed to the formation of Dy-O clusters, which introduce impurities into the semiconductor. As the doping concentration of rare earth oxide (Dy) increases, impurity levels rise, influencing the band structure.

At higher doping concentrations, impurity levels mostly overlap with the host metal oxide bands, significantly affecting the electronic structure. This leads to a further decrease in the effective band gap. In the case of MgNb<sub>2</sub>O<sub>6</sub> NPs, doping with Dy enhances the concentration of charge carriers, causing band gap narrowing due to many-body interactions, such as band tailing and electron–electron interactions. Furthermore, the introduction of nonbridging oxygen defects reduces the effective band gap by creating defect states, which facilitate additional electronic transitions within the band gap, allowing energy absorption at lower wavelengths [42].

Figure 5 depicts typical SEM images of 2%–8% Dy: MNbO NPs, showing their structural and surface morphologies. Since AV gel was used as fuel in the combustion synthesis of Dy: MNbO NPs, the SEM images reveal a soft, sponge-like and shimmering surface, along with clusters and a foam-like dispersion structure, indicating that the sample was formed via the combustion process.

Based on the results from the photocatalytic experiment, the 4 mol% Dy-doped MNbO NPs sample was selected for elemental analysis, as it exhibited better degradation performance compared to other molar percentages. The 4 mol %-Dy: MNbO NPs were further analysed using energy-dispersive X-ray (EDX) spectroscopy, as shown in Figure 5. The obtained data reveal that the prepared NPs contain Nb, O, Mg and Dy, and the atomic weight percentage of the elements in the sample is provided in the inset of Figure 6 [43].

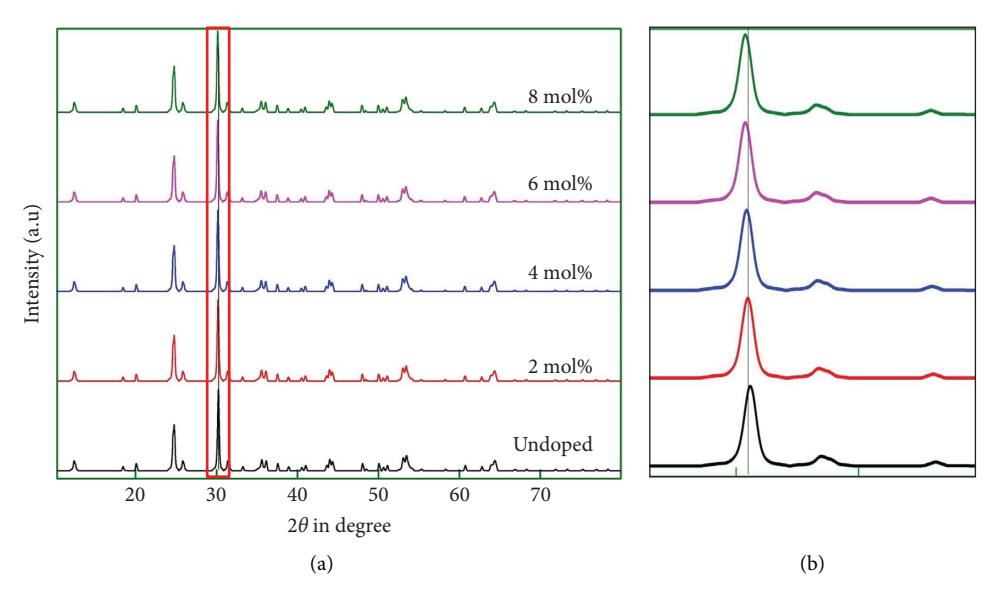


FIGURE 2: (a) XRD pattern of Dy: MNbO (0-8 mol%) NPs. (b) Exaggeration in the range from 25° to 40°.

Table 1: Crystalline size in nm and strain for plane (0 0 2) of Dy: MNbO (0-8 mol%) nanoparticle.

| The Dy (mol%) in concentration | 'D' (nm) | 'd' nm | $Dx \times 10^4 \text{ (kgm}^{-3}\text{)}$ | $\delta \times 10^{15} (\text{kgm}^{-3})^{-2}$ | $V \times 10^{-30} \text{ m}^3$ | SF   | $\varepsilon \ (\times \ 10^{-3})$ |
|--------------------------------|----------|--------|--|--|---------------------------------|------|------------------------------------|
| 0                              | 23       | 0.26   | 551.52                                     | 0.12   | 105.3                           | 0.56 | 1.48                               |
| 2                              | 25       | 0.29   | 591.37                                     | 0.19   | 123.5                           | 0.63 | 1.41                               |
| 4                              | 29       | 0.33   | 642.28                                     | 0.23   | 131.2                           | 0.69 | 1.32                               |
| 6                              | 36       | 0.39   | 651.70                                     | 0.256  | 138.2                           | 0.73 | 1.23                               |
| 8                              | 45       | 0.43   | 680.02                                     | 0.36   | 141.2                           | 0.89 | 1.13                               |

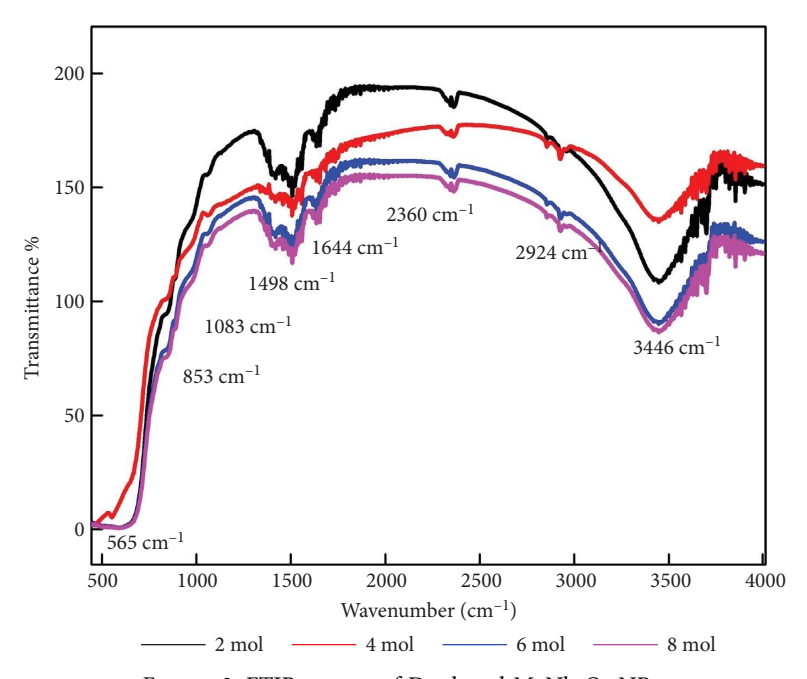


Figure 3: FTIR spectra of Dy-doped  $MgNb_2O_6$  NPs.

Figure 7(a) illustrates the TEM picture of 4 mol% prepared Dy: MNbO NPs with low-magnification image of 200 nm, which shows the irregularly shaped clustered NPs

and agglomerates of very small crystalline domains. The HR-TEM shown in Figure 7(b) of scale 10 nm depicts the possibly individual grains' development of highly crystalline

8384, 2025, 1, Downloaded from https://onlinelibrary.wieley.com/doi/10/115/jnt/6674176 by National Institutes Of Health Malaysia, Wiley Online Library on (05/11/2025]. See the Terms and Conditions (ttps://onlinelibrary.wiely.com/terms-and-conditions) on Wiley Online Library or rules of use; OA archies are governed by the applicable Centwive Commons License

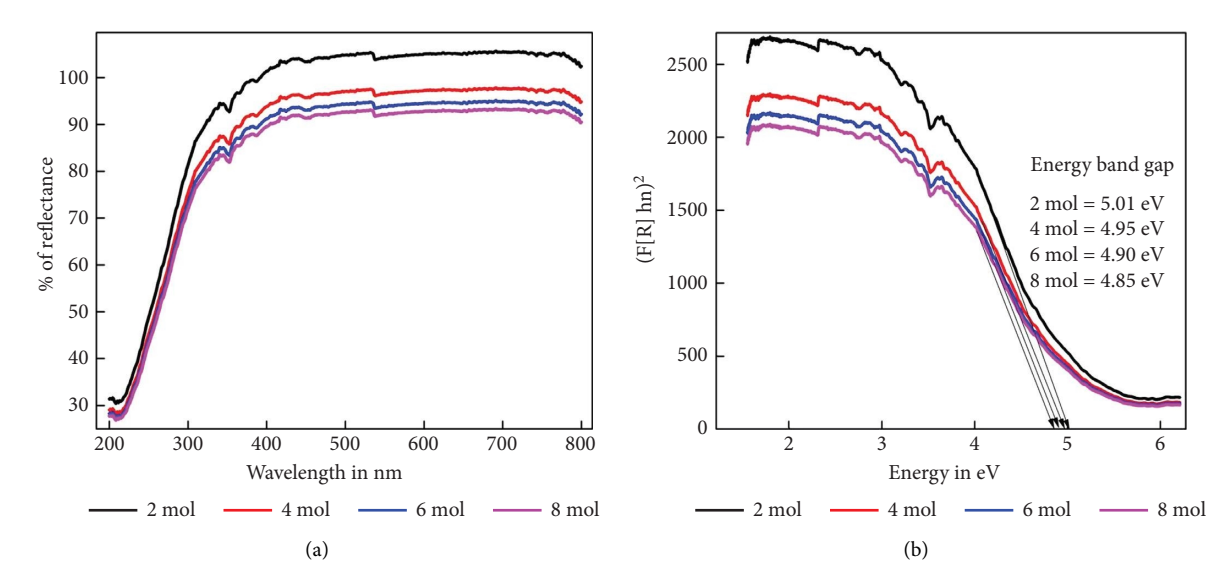


FIGURE 4: (a) Diffuse reflection spectra of spectral studies of Dy: MNbO and (b) Wood and Tauc's plot to find energy band gap.

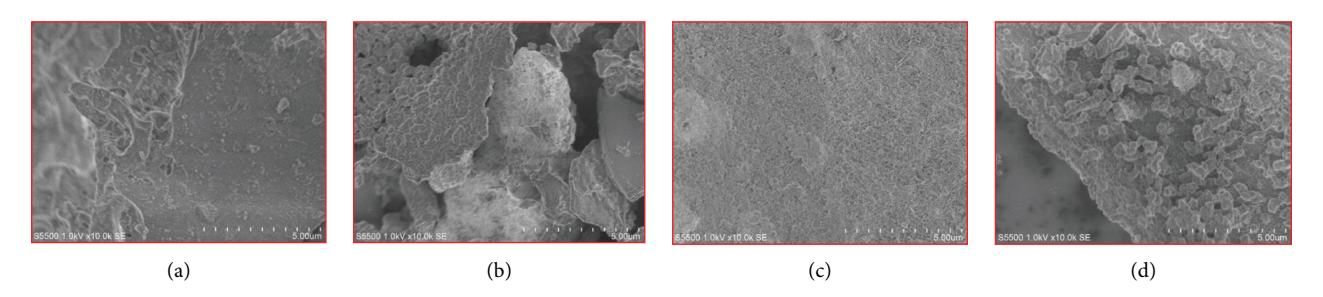


FIGURE 5: SEM micrographs different Dy concentration (a) 2 mol%, (b) 4 mol%, (c) 6 mol% and (d) 8 mol% of Dy: MNbO NPs.

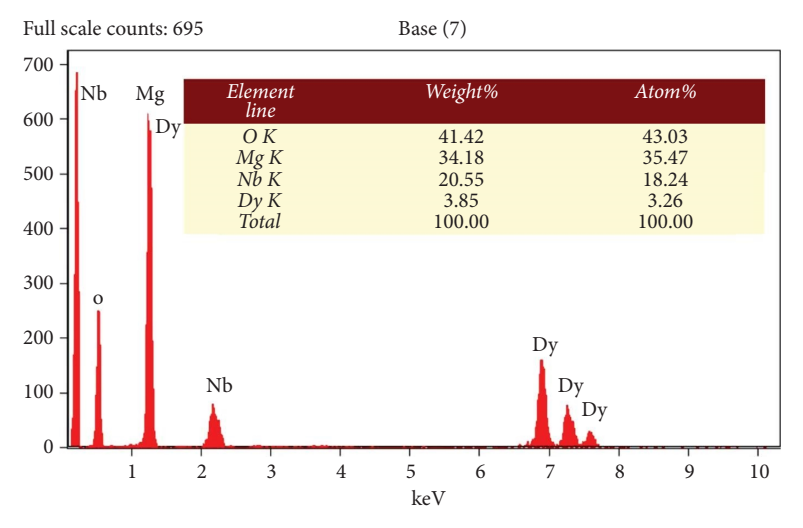


FIGURE 6: SEM-EDX reveals the elemental analysis for 4 mol% Dy: MNbO.

4 mol% Dy: MNbO NPs, and the visibility of lattice fringes is a clear indication that the material has a well-ordered crystalline structure at this scale, and SAED patterns shown in Figure 7(c) depict the development of surprising crystalline particles with ring-like structure [44, 45].

The absorbance spectra of a DG dye solution with varying molar concentrations of Dy-doped MgNb2O6 (Dy: MNbO) NPs as catalysts are shown in Figure 8. The percentage degradation of DG dye depends significantly on the molar concentration of Dy: MNbO NPs. For 2 mol% Dy:

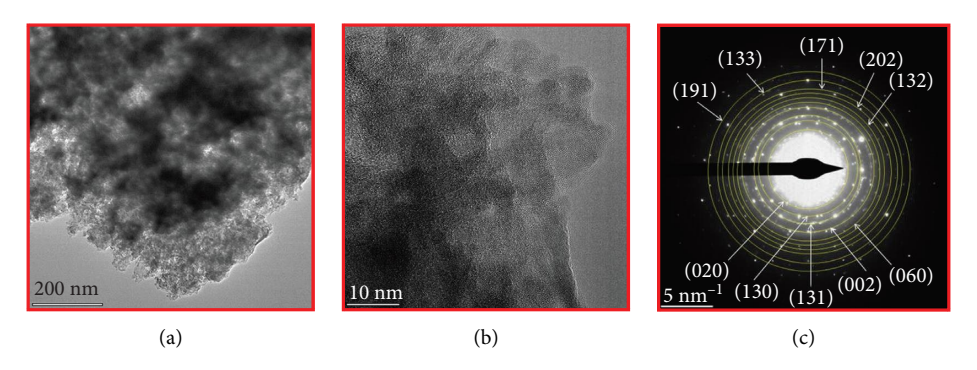


FIGURE 7: (a) TEM image, (b) HR-TEM, and (c) SAED of 4 mol% Dy: MNbO NPs.

MNbO NPs, the degradation efficiency is 69.65%, as shown in Figure 9(a). Increasing the concentration to 4 mol% enhances the degradation efficiency to 82.53% (Figure 9(b)). However, further increases to 6 mol% and 8 mol% result in reduced efficiencies of 78.82% and 76.09%, as shown in Figures 9(c), 9(d), respectively. These results demonstrate that 4 mol% Dy: MNbO NPs achieve the maximum degradation efficiency. And Table 2 summarizes the comparison of different studies on degradation efficiency [50]. The halflife of the DG dye, determined from the  $C/C_0$ , and  $1-C/C_0$ , versus time plots indicates the time required for half of the dye molecules to degrade under UV light. For 2 mol% Dy: MNbO NPs, the half-life is 49.36 s (Figure 10(a)), while for 4 mol%, it is 52.52 s (Figure 10(b)). At higher concentrations, the half-life is 50.54 s for 6 mol% (Figure 10(c)) and 36.54 s for 8 mol% (Figure 10(d)).

Further study of the reaction kinetics should be done to understand the degradation process. The pseudo-first-order kinetics model was applied using Equation (6). The degradation process, illustrated in Figure 11, shows a decrease in the  $C/C_0$  ratio over time, reflecting the declining concentration of the dye. Since  $C/C_0$  is less than 1, its logarithm is negative and approaches zero as the dye concentration stabilizes. The degradation occurs more rapidly at 4 mol% Dy: MNbO NPs, as indicated by the red curve, which exhibits a sharp decline between 45 and 75 min. This steeper curve signifies faster degradation kinetics compared to other molar concentrations.

The photocatalytic stability of the prepared Dy: MNbO NPs was also evaluated by performing repeated cycles of dye degradation. Figures 12(a), 12(b), 12(c) and 12(d) show that the degradation efficiency remains consistent during the first two cycles but decreases by up to 20% in the subsequent three cycles. These results suggest that Dy: MNbO NPs exhibit good stability, maintaining significant photocatalytic activity even after multiple reuse cycles [51].

$$\log\left(\frac{C}{C_0}\right) = -kt,\tag{6}$$

where C is the concentration of the substance at time t,  $C_0$  is the initial concentration, k is the pseudo-first-order rate constant, and t is the time.

3.1. Mechanism of Photodegradation. Mechanism of DG dye with the penetration of UV light of energy (hv) on Dy: MNbO NPs with dye molecule is shown in Figure 13. In this process, Dy ions in higher oxidation states can introduce localized energy levels within the band gap of the photocatalytic material. These energy levels can capture excited electrons (e-) in the valence band, which get energized and exited to the conduction band with penetration of energy, which is greater than or equal to energy band gap. Therefore, electron and hole pairs are created. By trapping the electrons, Dy prevents them from recombining with holes (h<sup>+</sup>) in the valence band and it is reacted by surrounding oxygen and generates anion radicals  $(O^{2-})$ . At the same time, holes in the valence band can oxidize dye directly or produce hydroxyl radicals (OH<sup>-</sup>) from adsorbed water molecules. In this process, the active hydroxyl radicals are OH and super oxide radicals O<sup>2-</sup> are oxidized with adsorbed dye molecules, because the exited electrons and holes are degraded the dye sample [52, 53].

The efficiency of this photocatalytic process is influenced by the Dy doping concentration, which affects the surface morphology and active site density of MgNb<sub>2</sub>O<sub>6</sub>. An optimal concentration of Dy enhances surface activity, facilitating the generation of active radicals and improving the photocatalytic degradation. However, excessive Dy doping can block active sites. Among the tested concentrations, 4 mol% Dy-doped MgNb<sub>2</sub>O<sub>6</sub> showed the highest degradation rate of the DG dye solution, outperforming the 2 mol%, 6 mol% and 8 mol% Dy-doped samples due to its optimal balance of active sites and surface reactivity.

The steps involved in the photodegradation process are presented in equations (2)–(6).

MNbO: Dy + 
$$hv \longrightarrow$$
 MNbO: Dy\*,  
MNbO: Dy\*  $\longrightarrow$  MNbO: Dy  $(h^+ + e^-)$ ,  
MNbO: Dy\*  $(e^-) + O_2 \longrightarrow O^{2^{--}}$ , (7)  
 $O^{2^{--}} + H_2O \longrightarrow OH + OH^{--}$ ,  
 $OH^{--} + O^{2^{--}} + Dye \longrightarrow degraded water.$ 

For electrochemical CV testing, the 4 mol% Dy: MNbO NPs served as a modified working electrode. The electrodes operate in 0.1 N HCL as a electrolyte at the scan rate which

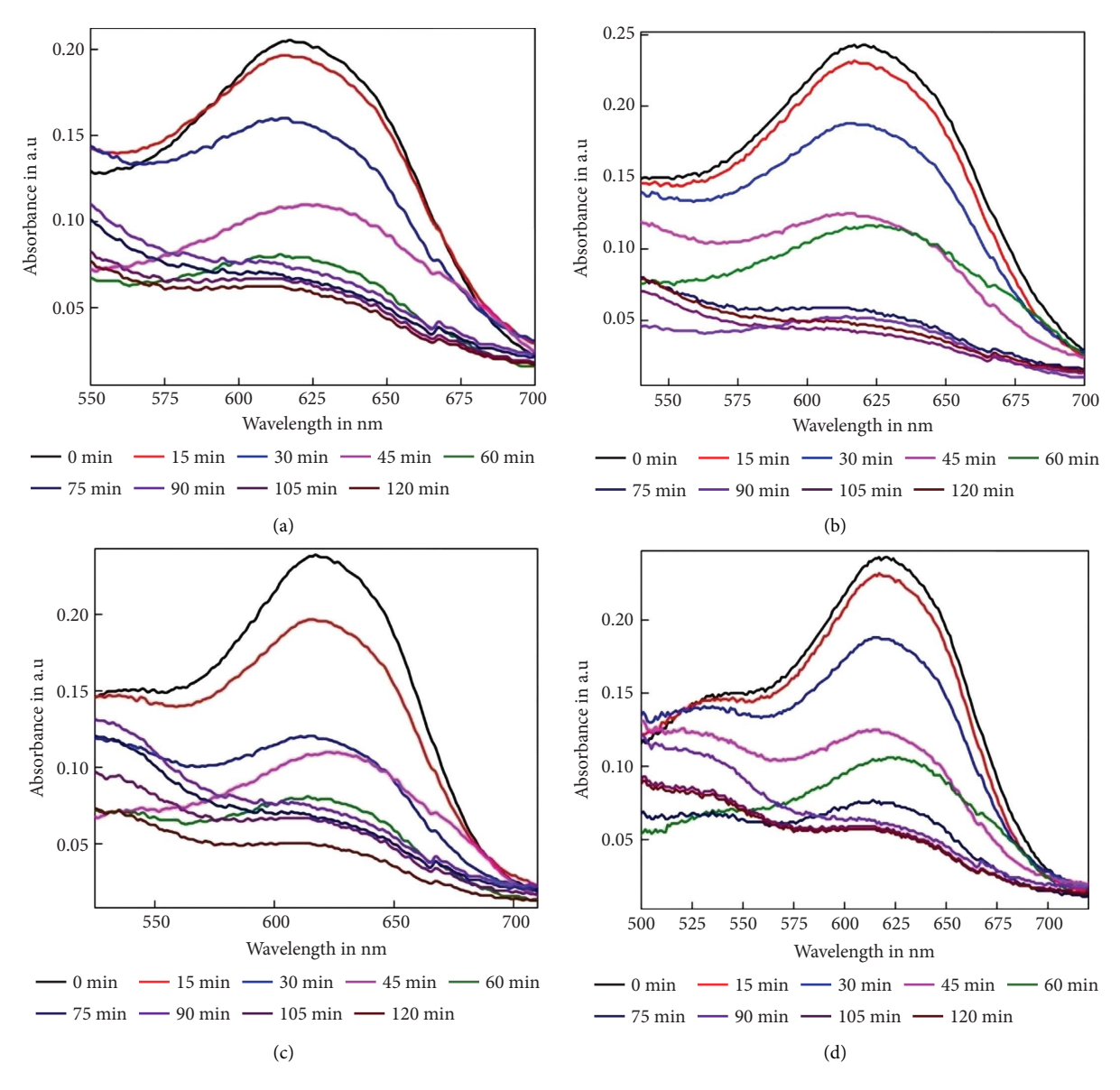


FIGURE 8: Absorption spectra DG dye irradiated with UV light to catalyst of (a) 2 mol%, (b) 4 mol%, (c) 6 mol% and (d) 8 mol% of Dy: MNbO NPs.

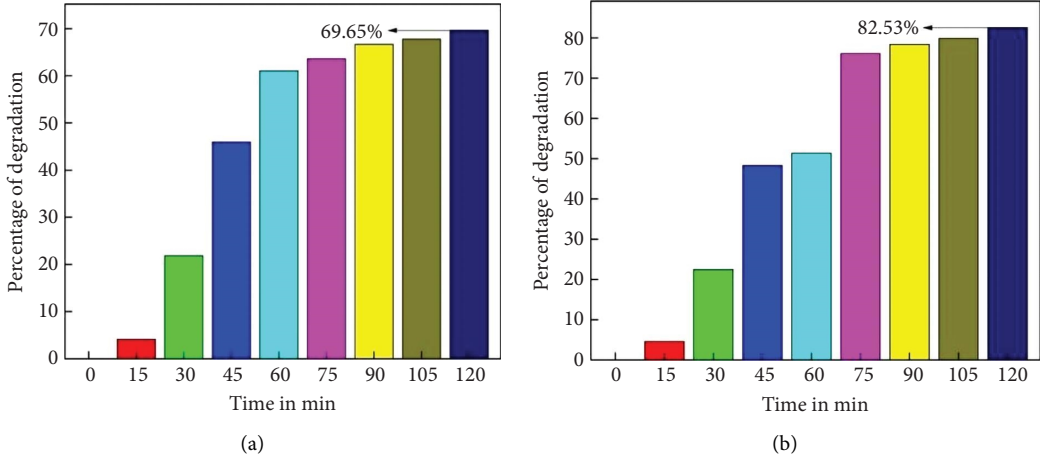


FIGURE 9: Continued.

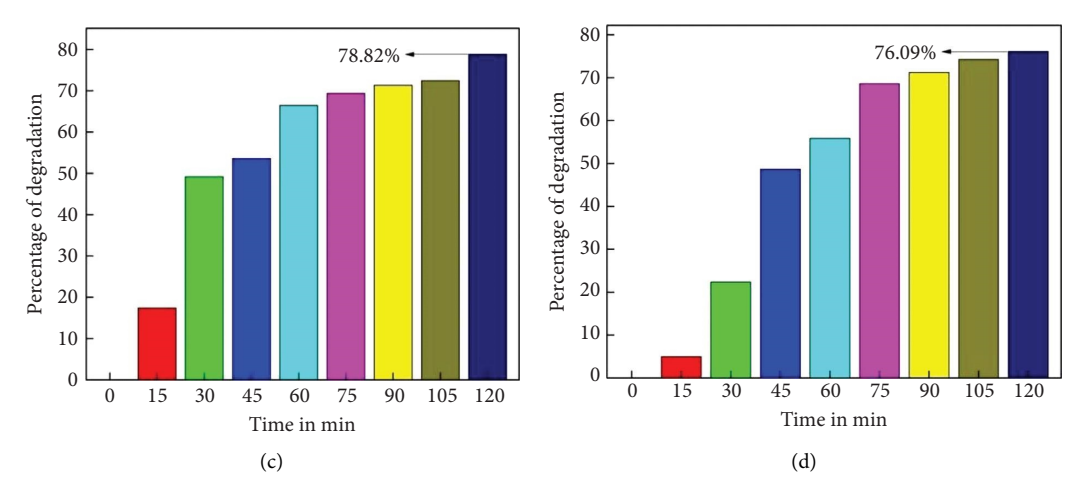


FIGURE 9: Percentage degradation of DG dye under UV light of (a) 2 mol%, (b) 4 mol%, (c) 6 mol% and (d) 8 mol% of Dy: MNbO NPs.

Table 2: Comparison of previous studies on photodegradation of Dy dopants.

| S. no | Fuel used<br>in synthesis<br>NPs | Nanoparticles                      | Method of preparation    | Dye/pollutant         | % degradation<br>(%) | References |
|-------|----------------------------------|------------------------------------|--------------------------|-----------------------|----------------------|------------|
| 1     | Green fuel                       | Present work                       | Combustion synthesis     | Direct green (DG) dye | 82                   | _          |
| 2     | Chemical fuel                    | MgCaNb <sub>2</sub> O <sub>6</sub> | Solid solution           | Phenol                | 78                   | [46]       |
| 3     | Chemical fuel                    | Dy-doped ZnO                       | Chemical spray pyrolysis | Methylene blue        | 92                   | [47]       |
| 4     | Chemical fuel                    | Dy-doped TiO <sub>2</sub>          | Hydrothermal treatment   | Methylene blue        | 98.72                | [48]       |
| 5     | Green fuel                       | Dy-doped ZnO                       | Sonochemical method      | Methylene blue        | 58-98                | [49]       |

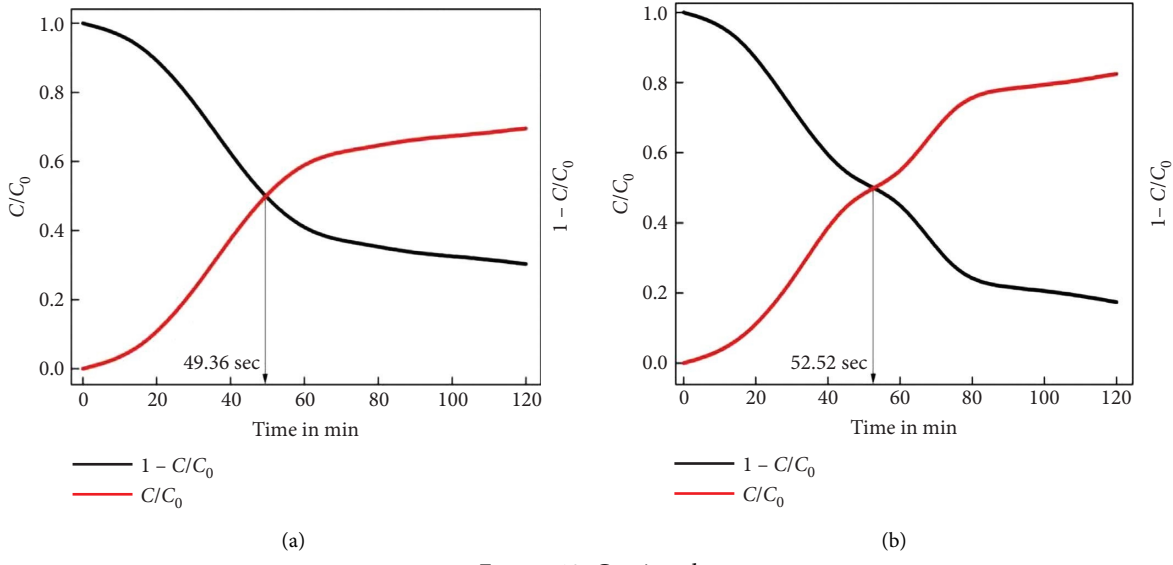


Figure 10: Continued.

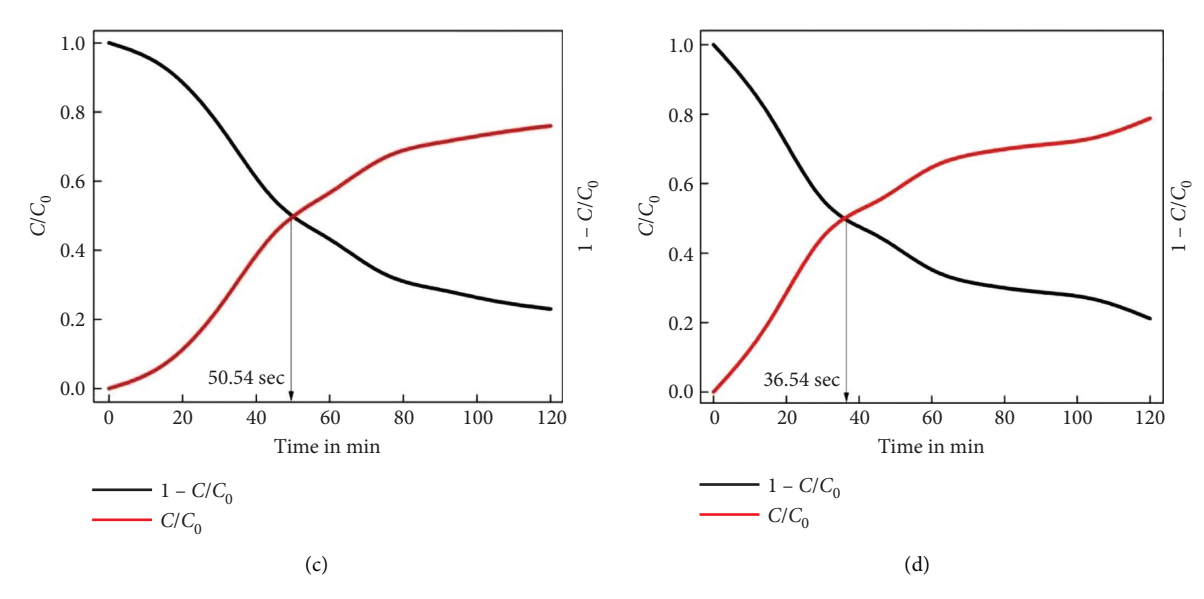


FIGURE 10: Half-life DG dye under UV light irradiation with (a) 2 mol%, (b) 4 mol%, (c) 6 mol% and (d) 8 mol% of Dy: MNbO NPs as a catalyst.

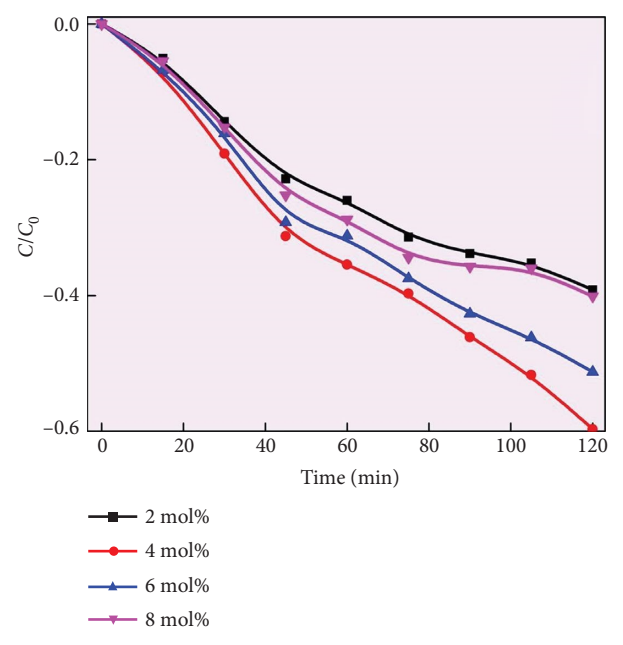


FIGURE 11: The plots of  $C/C_0$  versus time.

varies from 10 to  $50\,\mathrm{mVs^{-1}}$ . Within the conceivable spectrum range of -1.2 to  $0.4\,\mathrm{V}$ , the CV is shown in Figure 14(a). There are smaller oxidation peaks at  $-0.28\,\mathrm{V}$  and  $-0.022\,\mathrm{V}$  and reduction peaks at  $-0.54\,\mathrm{V}$  due to oxidation and reduction of Mg ions. There is a minor variation observed in the positions of the anodic and cathodic peaks of the electrode as the cycle progresses, indicating excellent electrode stability [54, 55].

Figure 14(b) depicts the correlation between the square root of the scan rate ( $v^{1/2}$ ) and the cathodic peak current (ip) for 4 mol% Dy: MNbO NP electrode. The stronger linear relationship between ip and  $v^{1/2}$  demonstrates that hydrogen diffusion limits the electrode reactivity of 4 mol% Dy: MNbO

NP electrode. The hydrogen diffusion coefficient of the 4 mol % Dy: MNbO NP electrode is determined to be  $9.30 \times 10^{-5}$  cm<sup>2</sup>s<sup>-1</sup> using the slope of the fitted line followed by Equation (8).

ip = 
$$2.69 \times 10^5 \times n^{3/2} \times A \times D^{1/2} \times C_o \times v^{1/2}$$
. (8)

Since the complex electric modulus formalism has the advantage of suppressing electrode polarizing effects, it is commonly used to examine the electrical relaxation in ionically and electrically conducting materials [56]. Equation (9) provided the real and imaginary components of the complex electric modulus. The one semicircle on the Nyquist

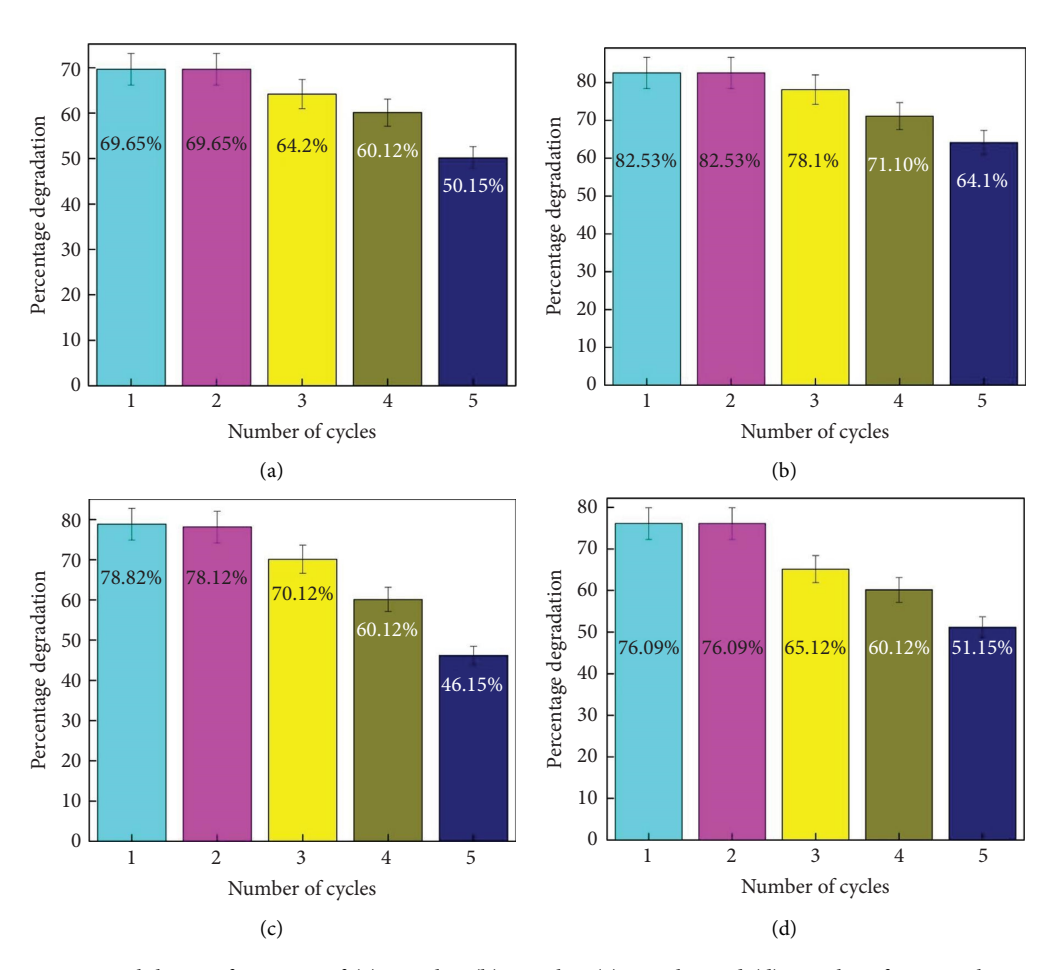


FIGURE 12: Stability performance of (a) 2 mol%, (b) 4 mol%, (c) 6 mol% and (d) 8 mol% of Dy: MNbO NPs.

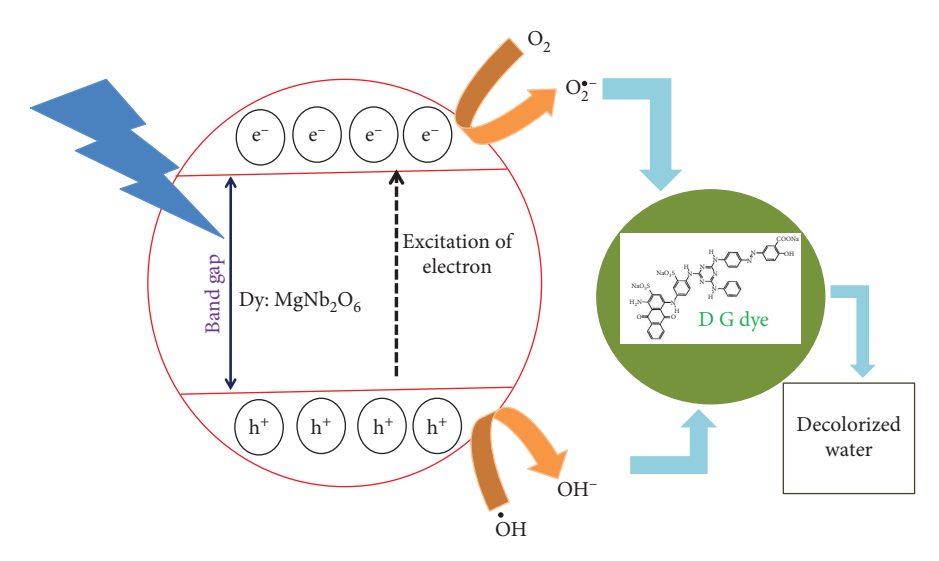


FIGURE 13: The photocatalytic degradation mechanism of DG dye degradation.

or Cole-Cole plots is often attributed to the resistances resulting from grain borders, grain size and electrode impact, in that order. The impedance spectra of 4 mol% Dy: MNbO NPs are shown in Figure 14(c) [57]. From the equivalent circuit (inset of Figure 14(c)), the obtained  $R_{ct}$  and  $C_{dl}$  values are  $78.85\,\Omega$  and  $0.0001886\,F.$ 

$$Z(W) = Z' + Z'' = Z_{Re} + jZ_{Im} = R + jX.$$
 (9)

It shows the relationship between the applied potential and the resulting current as a function of frequency. The Bode plot is obtained plotting phase angle v/s logarithm of frequency shown in Figure 14(d). The phase angle is 64°,

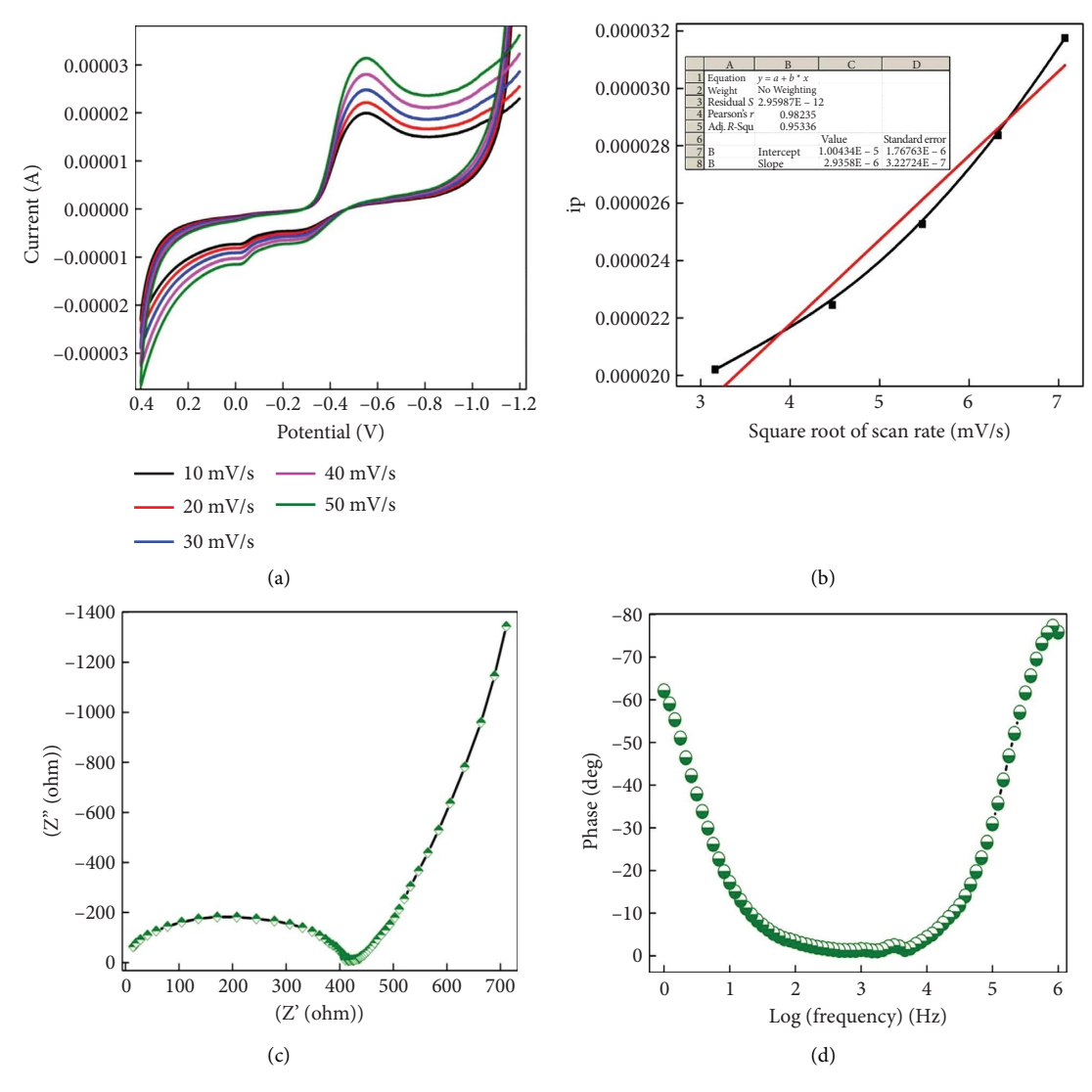


FIGURE 14: (a) CV of 4 mol% Dy: MNbO nanoparticles. (b): Relationship between the cathodic peak current (ip) and the square root of scan rate of Dy: MNbO electrode. (c) Nyquist plot with equivalent circuit (inset). (d) Bode plot for Dy: MNbO electrode.

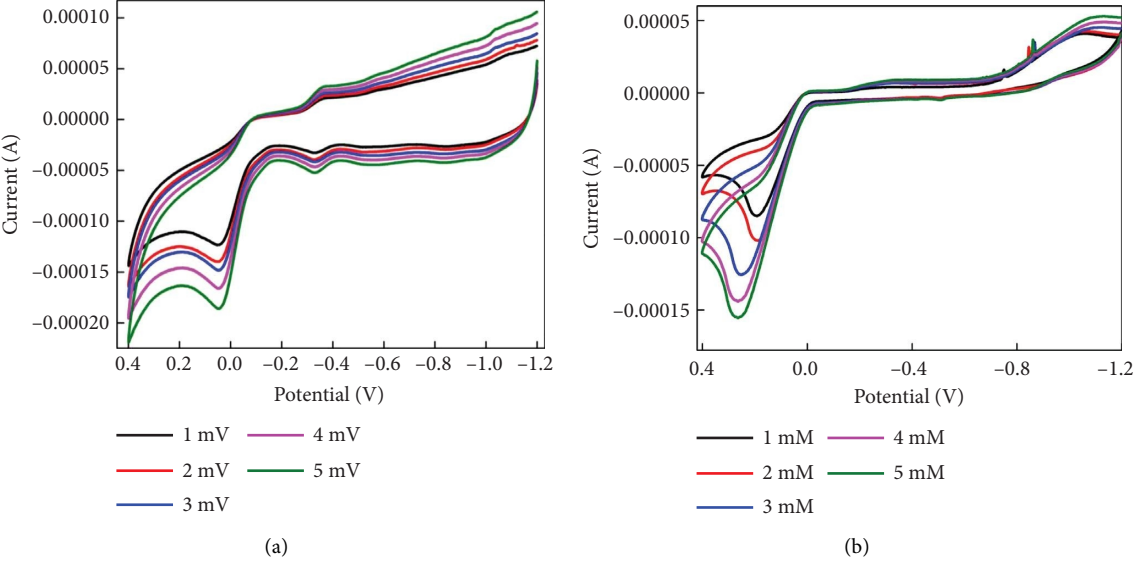


FIGURE 15: Continued.

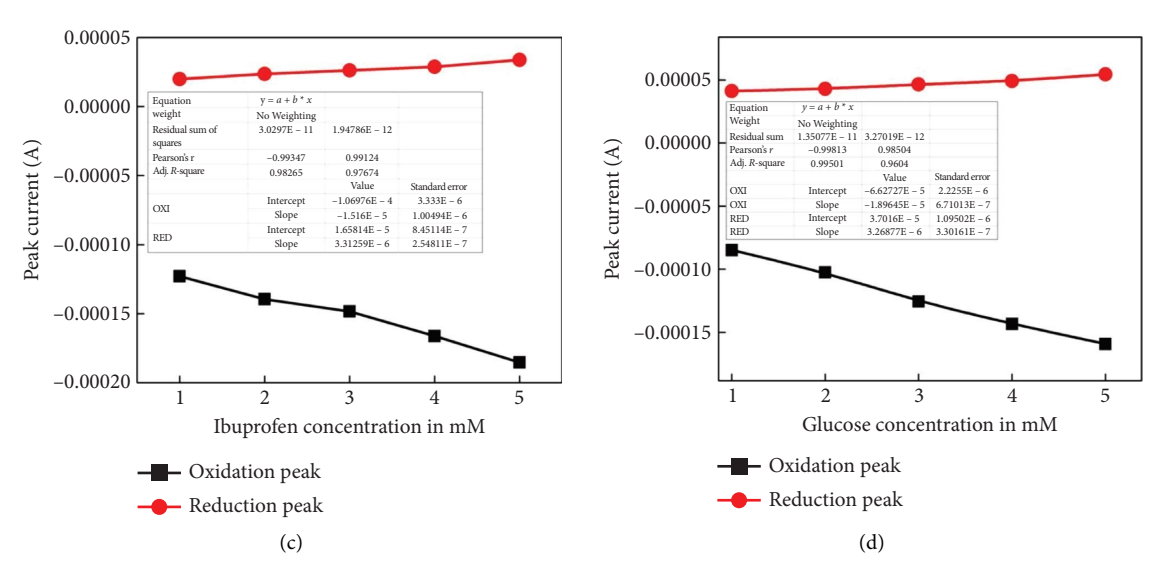


FIGURE 15: (a) CV plot of 4 mol% Dy: MNbO NPs sensing ibuprofen (concentration range 1–5 mM), (b) CV plot of 4 mol% Dy: MNbO in the sensing of glucose (concentration range 1–5 mM). (c), (d) calibration plot of current response v/s concentration of ibuprofen and glucose with fitted line.

which is close to current and leads the applied potential by a phase angle of (90°) degrees, indicating capacitive behaviour. At high frequencies, the system behaves more like a pure capacitor.

The sensor performance of the Dy: MNbO electrode was used to detect the ibuprofen and d-glucose in 0.1 M HCl solution as shown in Figures 15(a) and 15(b), respectively. In the CV graph, variations in oxidation and reduction peaks were observed after adding the mile-molar concentration of ibuprofen and glucose to electrolyte solution of dosage from 1 to 5 Mm, and the prepared modified Dy: MNbO electrode exhibited sensing ability. In ibuprofen sensor, a clear oxidation peak is visible at 0.045 V, and the reduction peak is less prominent, whereas in d-glucose sensor, a oxidation peak is visible at 0.265 V. Successive injections of 1 mM ibuprofen or d-glucose at 50-s intervals resulted in a rapid increase in current response, reaching a steady state within 3 s.

In Figures 15(c) and 15(d), the peak current was plotted against the concentrations of ibuprofen and glucose using the calibration curve. The Dy: MNbO electrode exhibited a low detection limit of  $1 \times 10^{-3}$  mol/L. The linearity of the calibration curve also suggests that the activity is diffusion-controlled within the reported concentration range [58]. This further supports the enhanced sensitivity of Dy: MNbO modified electrodes toward the detection of glucose and ibuprofen. Further, the proposed sensor was employed to determine the ibuprofen and glucose ions in water and showed sensitivity in the order of 0.005 and 0.006 A. Lastly, a high surface area improves contact with analyte molecules and expands the number of active sites accessible for photocatalytic processes, increasing sensor sensitivity and response time. Additionally, when a material interacts with target molecules, its electrical conductivity changes, which is a crucial mechanism in many gas or chemical sensors. Semiconducting qualities also affect the material's capacity to absorb light and catalyse reactions.

#### 4. Conclusions

Cost effective Dy: MNbO NPs were synthesized using AV gel as a biofuel through a solution-based green combustion process. These Dy: MNbO NPs were specifically designed for dual applications, serving as efficient photocatalysts and as materials for electrochemical cyclic voltammetry (CV) and sensing studies. The incorporation of dysprosium (Dy) plays a crucial role in enhancing the material's functionality by reducing electron-hole recombination and promoting effective charge carrier separation. Additionally, Dy doping alters the electronic properties of MNbO, improving both light absorption and electrical conductivity. These improvements result in a higher availability of charge carriers, which significantly boosts the material's photocatalytic and electrochemical performance. The characterization of the prepared NPs revealed their orthorhombic phase structure, with an average crystallite size of about 45 nm, and an energy band gap ranging from 4.85 to 5.01 eV, respectively. The exceptional attributes of the synthesized NPs, including high conductivity, porous morphology, swift charge transfer capabilities, and photosensitivity, were explored. Notably, the Dy: MNbO (4 mol%) material exhibited appreciable photocatalytic activity, achieving a remarkable 82.53% degradation of DG dye under UV light, because 4 mol% of Dy: MNbO NPs show excellent performance in photodegradation, which is an evident for good number of electrons and holes that participate in oxidation and reduction reactions to degrade pollutants compared to 2 mol, 6 mol and 8 mol% NPs with a calculated half-life of 50.54 min. Furthermore, 4 mol% of Dy: MNbO NPs show the anodic and cathodic peaks in electrochemical CV studies that reveals the good electrode stability, and diffusion coefficient of the electrode is determined to be  $9.30 \times 10^{-5}$  cm<sup>2</sup>s<sup>-1</sup>; the Nyquist plots are often one semicircle that attributed to the resistances Dy: MNbO NPs, and the

Bode plot is obtained with phase angle of 64° indicating capacitive behaviour. The electrochemical sensor study is utilized to demonstrate high sensitivity, in enabling the detection of ibuprofen drug and glucose concentrations at 1 mM, in an acidic electrolyte solution of 0.1M HCl. The Dy: MNbO NP findings highlight the usefulness and cost efficiency of NPs as a promising material for catalysis and sensing applications. With the utilization of AV as a green fuel in synthesizing practices, this emphasizes the promising potential of Dy: MNbO NPs for a range of real-world applications.

# **Data Availability Statement**

The data that support the findings of this study are available from the corresponding author upon reasonable request.

#### **Ethics Statement**

The authors have nothing to report.

#### **Consent**

The authors have nothing to report.

## **Conflicts of Interest**

The authors declare no conflicts of interest.

#### **Author Contributions**

N. Basavaraju: data curation and investigation. H. N. Shwetha: data curation and methodology. C. R. Ravikumar: funding acquisition, supervision, resources and writing – original draft. Syed Khasim: software and validation. K. B. Tan: formal analysis. Kiflom Gebremedhn Kelele: methodology. K. Y. Chan: visualization and writing – review and editing. H. C. Ananda Murthy: conceptualization, resources and writing – review and editing.

#### **Funding**

No funds received.

#### References

- [1] S. Elhenawy, M. Khraisheh, F. AlMomani, M. Al-Ghouti, R. Selvaraj, and A. Al-Muhtaseb, "Emerging Nanomaterials for Drinking Water Purification: A New Era of Water Treatment Technology," *Nanomaterials* 14, no. 21 (2024): 1707, https://doi.org/10.3390/nano14211707.
- [2] Z. Alhalili, "Metal Oxides Nanoparticles: General Structural Description, Chemical, Physical, and Biological Synthesis Methods, Role in Pesticides and Heavy Metal Removal Through Wastewater Treatment," *Molecules* 28, no. 7 (2023): 3086, https://doi.org/10.3390/molecules28073086.
- [3] M. Wang, B. L. Bodirsky, R. Rijneveld, et al., "A Triple Increase in Global River Basins With Water Scarcity Due to Future Pollution," *Nature Communications* 15, no. 1 (2024): 880, https://doi.org/10.1038/s41467-024-44947-3.
- [4] P. Kumar, N. Thakur, K. Kumar, et al., "Catalyzing Innovation: Exploring Iron Oxide Nanoparticles—Origins,

- Advancements, and Future Application Horizons," *Coordination Chemistry Reviews* 507 (2024): 215750, https://doi.org/10.1016/j.ccr.2024.215750.
- [5] M. Tripathy, P. Aparajita, S. Pattnayak, G. Hota, and A. K. Ghosh, "Chapter 14—Nanotechnology-Based Sustainable Approaches for Remediation of Organic and Inorganic Pollutants from Aqueous Medium," Water, the Environment, and the Sustainable Development Goals, ed. M. H. Dehghani, R. Rao Karri, I. Tyagi, and M. Scholz (Elsevier, 2024), 327–355, https://doi.org/10.1016/B978-0-443-15354-9.00015-3.
- [6] R. K. Mishra, "Fresh Water Availability and Its Global Challenge," *British Journal of Multidisciplinary and Advanced Studies* 4, no. 3 (2023): 1–78, https://doi.org/10.37745/bjmas.2022.0208.
- [7] T. Akter, A. T. Protity, M. Shaha, M. Al Mamun, and A. Hashem, "The Impact of Textile Dyes on the Environment," in *Nanohybrid Materials for Treatment of Textiles Dyes: Smart Nanomaterials Technology*, ed. A. Ahmad, M. Jawaid, M. N. Mohamad Ibrahim, A. A. Yaqoob, and M. B. Alshammari (Springer, 2023), https://doi.org/10.1007/ 978-981-99-3901-5\_17.
- [8] S. Aziz, A. R. Mazhar, A. Ubaid, et al., "A Comprehensive Review of Membrane-Based Water Filtration Techniques," *Applied Water Science* 14, no. 8 (2024): 169, https://doi.org/ 10.1007/s13201-024-02226-y.
- [9] N. A. Abd El-Ghany, M. H. A. Elella, H. M. Abdallah, M. S. Mostafa, and M. Samy, "Recent Advances in Various Starch Formulation for Wastewater Purification Via Adsorption Technique: A Review," *Journal of Polymers and the Environment* 31, no. 7 (2023): 2792–2825, https://doi.org/ 10.1007/s10924-023-02798-x.
- [10] M. S. Chauhan, A. K. Rahul, S. Shekhar, and S. Kumar, "Removal of Heavy Metal From Wastewater Using Ion Exchange With Membrane Filtration From Swarnamukhi River in Tirupati," *Materials Today: Proceedings* 78, no. Part 1 (2023): 1–6, https://doi.org/10.1016/j.matpr.2022.08.280.
- [11] Q. Wu, C. Chen, Y. Zhang, et al., "Safe Purification of Rural Drinking Water by Biological Aerated Filter Coupled with Ultrafiltration," *Science of the Total Environment* 868 (2023): 161632, https://doi.org/10.1016/j.scitotenv.2023.161632.
- [12] A. Knap-Bałdyga, "Monika Żubrowska-Sudoł Natural Organic Matter Removal in Surface Water Treatment Via Coagulation—Current Issues, Potential Solutions, and New Findings Department of Water Supply and Wastewater Treatment, Faculty of Building Services, Hydro, and Environmental Engineering," Warsaw University of Technology, Nowowiejska 20, 00-653 Warsaw, Poland 15, no. 18 (2023): 13853, https://doi.org/10.3390/su151813853.
- [13] X. Chen, J. Ma, J. Chen, and Z. Wang, "Ceramic Membrane Filtration Coupled With Ozonation for Water Purification: Principles, Applications and Perspectives," *Journal of Water Process Engineering* 55 (2023): 104127, https://doi.org/ 10.1016/j.jwpe.2023.104127.
- [14] M. Giridhar, B. C. Manjunath, K. Gurushantha, et al., "Influence of Zr on the Sun-Light Driven Photocatalytic Activity, Electrochemical Sensor, and Microbial Applications of CuFe<sub>2</sub>O<sub>4</sub> NPs," Sensing Technology 2, no. 1 (2024): 2417721, https://doi.org/10.1080/28361466.2024.2417721.
- [15] S. B. Surendra, K. N. Harish, T. Kiran, K. K. Prasanth, M. V. Chethana, and V. V. Shanbhag, "Effect of Developed NiFe<sub>2</sub>O<sub>4</sub> NPs for Electrochemical Sensing Action on Ascorbic Acid Detection and Photocatalytic Applications," *Ionics* 31, no. 2 (2024): 2189–2204, https://doi.org/10.1007/s11581-024-05994-4.

[16] Z. Hou, W. Pei, X. Zhang, et al., "Rare Earth Oxides and Their Supported Noble Metals in Application of Environmental Catalysis," *Journal of Rare Earths* 38, no. 8 (2020): 819–839, https://doi.org/10.1016/j.jre.2020.01.011.

- [17] G. Maduraiveeran, M. Sasidharan, and W. Jin, "Earth-Abundant Transition Metal and Metal Oxide Nanomaterials: Synthesis and Electrochemical Applications," *Progress in Materials Science* 106 (2019): 100574, https://doi.org/10.1016/j.pmatsci.2019.100574.
- [18] D. Yu, Q. Ding, T. Shen, et al., "Broadband Short-Wave Near-Infrared-Emitting Phosphor MgNb<sub>2</sub>O<sub>6</sub>: Cr<sup>3+</sup> for Pc-LED Applications," *Dalton Transactions* 53, no. 8 (2024): 3702–3712, https://doi.org/10.1039/D3DT03896C.
- [19] N. Basavaraju, N. Raghavendra, T. A. Hamdalla, et al., "A Novel Synthesis of ZnNb<sub>2</sub>O<sub>6</sub> Nanoparticles Via Combustion Method: Supercapacitor and Photocatalytic Properties," Particle & Particle Systems Characterization 41, no. 12 (2024): https://doi.org/10.1002/ppsc.202400061.
- [20] Z. Huang, J. Qiao, and L. Li, "Enhanced Dielectric Properties and Chemical Bond Characteristics of MgNb<sub>2</sub>O<sub>6</sub> Ceramics Due to Magnesium Oxide Doping," *Ceramics International* 49, no. 20 (2023): 32946–32952, https://doi.org/10.1016/j.ceramint.2023.07.269.
- [21] S. Irtiqa and A. Rahman, "Photocatalytic and Photoluminescence Studies of La, Ce, and Dy Co-Doped ZnO Nanoflowers," *Journal of The Institution of Engineers (India): Series E* 103, no. 2 (2022): 259–270, https://doi.org/10.1007/s40034-021-00233-1.
- [22] V. G. Kessler and G. A. Seisenbaeva, "Molecular Mechanisms of the Metal Oxide Sol-Gel Process and Their Application in Approaches to Thermodynamically Challenging Complex Oxide Materials," *Journal of Sol-Gel Science and Technology* 107, no. 1 (2023): 190–200, https://doi.org/10.1007/s10971-023-06120-y.
- [23] Y. Abbas, H. F. Kiani, and M. Anis-ur-Rehman, "Investigation of High-Temperature Transport Mechanism and Dielectric Properties of RE-Double-Doped Perovskite Cobaltite Using Co-Precipitation Technique," *Journal of Molecular Structure* 1305 (2024): 137710, https://doi.org/10.1016/j.molstruc.2024.137710.
- [24] M. Ishfaq, M. Aadil, R. E. Syeda, et al., "Synthesis of Binary Metal Doped CeO<sub>2</sub> Via the Subcritical Hydrothermal Method for Photo-Mineralizing Methyl Orange Dye," *Journal of Alloys* and Compounds 960 (2023): 170661, https://doi.org/10.1016/ j.jallcom.2023.170661.
- [25] B. Basha, M. Ikram, Z. A. Alrowaili, M. S. Al-Buriahi, M. Anwar, and M. Suleman, "Wet Chemical Route Synthesis of Cr Doped CoFe<sub>2</sub>O<sub>4</sub> @rGO Nanocomposite for Photodegradation of Organic Effluents Present in Drinking Water," *Ceramics International* 49, no. 18 (2023): 30049–30059, https://doi.org/10.1016/j.ceramint.2023.06.262.
- [26] M. Misevicius, E. Griniuk, and R. Ramanauskas, "Solid-State Synthesis of LiYGeO<sub>4</sub> and Luminescence Properties of Dy-Doped Samples," *Materials Chemistry and Physics* 306 (2023): 128082, https://doi.org/10.1016/j.matchemphys.2023.128082.
- [27] N. Sharma and P. P. Sahay, "Solution Combustion Synthesis of Dy-Doped ZnO Nanoparticles: An Investigation of Their Structural, Optical and Photoluminescence Characteristics," *Journal of Luminescence* 257 (2023): 119655, https://doi.org/ 10.1016/j.jlumin.2022.119655.
- [28] N. Nasir Ahamed, J. Pattar, M. R. Anil Kumar, et al., "Electro-Chemical Studies of Zn Doped Nickel Oxide Nanoparticles Synthesized Via Solution Combustion Method Using Green

- and Chemical Fuels," *RSC Advances* 14, no. 25 (2024): 17664–17674, https://doi.org/10.1039/D4RA01706D.
- [29] S. Yadav, A. Khan, and J. G. Sharma, "Phytochemistry of Aloe Vera: A Catalyst for Environment-Friendly Diverse Nanoparticles With Sustained Biomedical Benefits," *Nature Envi*ronment and Pollution Technology 24, no. 1 (2025): B4182, https://doi.org/10.46488/nept.2025.v24i01.b4182.
- [30] S. Singh and B. Jain, "Green Synthesis of Zinc Oxide Nanoparticles Using Aloe Vera: A Study on Optical Properties and Photocatalytic ACTIVITY," *ChemRxiv* (2024): https://doi.org/10.26434/chemrxiv-2024-83hjj.
- [31] N. S. F. Dzulkharnien, R. Rohani, and H. A. Radzuan, "Comparative Analysis: Particle Size and Bactericidal Efficacy of Zinc Oxide Nanoparticles With Aloe Vera Gel Versus Aloe Vera Gel-Honey," *Physica Scripta* 99 (2024): https://doi.org/ 10.1088/1402-4896/ad5f59.
- [32] A. Basavaraja, C. R. Ravikumar, A. A. Khan, et al., "A Sustainable Combustion Process for Green Synthesis of TiO<sub>2</sub> Nanoparticles: Applications in Photocatalytic Degradation and Electrochemical Sensing for Environmental Remediation," *ChemistrySelect* 9, no. 14 (2024): https://doi.org/10.1002/slct.202304910.
- [33] S. N. Manjula, M. Chandrasekhar, M. R. Anil Kumar, et al., "Synthesis of MgAl<sub>2</sub>O<sub>4</sub>: Sm<sup>3+</sup> Nanophosphor and its Photoluminescence, Electrochemical Sensing, and Photocatalytic Studies First," *Advances in Materials Science and Engineering* 2023 (2023): 1–15, https://doi.org/10.1155/2023/8818883.
- [34] J. Y. Si, S. Y. Song, N. Liu, G. M. Cai, and L. M. Su, "Synthesis and Photoluminescence of Host-Sensitized MgNb<sub>2</sub>O<sub>6</sub> Based Phosphors," *Journal of Luminescence* 198 (2018): 10–18, https://doi.org/10.1016/j.jlumin.2018.02.014.
- [35] L. Li, G. Feng, D. Wang, et al., "Optical Floating Zone Method Growth and Photoluminescence Property of MgNb<sub>2</sub>O<sub>6</sub> Crystal," *Journal of Alloys and Compounds* 509, no. 27 (2011): L263–L266, https://doi.org/10.1016/j.jallcom.2011.04.063.
- [36] P. Klug and L. E. Alexander, X-Ray Diffraction Procedure (Wiley, 1954).
- [37] L. Srisombat, S. Ananta, and S. Phanichphant, "Chemical Synthesis of Magnesium Niobate Powders," *Materials Letters* 58, no. 6 (2004): 853–858, https://doi.org/10.1016/j.matlet.2003.07.024.
- [38] M. Chen, X. Wang, and Q. Qin, "Characterization of the Products Generated From Laser Ablation of Nb<sub>2</sub>O<sub>5</sub> Using Matrix Isolation FTIR Spectroscopy," *Applied Surface Science* 156, no. 1–4 (2000): 16–20, https://doi.org/10.1016/S0169-4332(99)00511-5.
- [39] P. Kubelka and F. Munk, "Ein Beitrag Zur Optik der Farbanstriche, Z," *Technical Physics* 12 (1931): 593–601.
- [40] C. Zaldo, M. J. Martin, C. Coya, K. Polgar, A. Peter, and J. Paitz, "Optical Properties of MgNb<sub>2</sub>O<sub>6</sub> Single Crystals: A Comparison With LiNbO<sub>3</sub>," *Journal of Physics: Condensed Matter* 7 (1995): 2249–2257, https://doi.org/10.1088/0953-8984/7/11/002.
- [41] Y. Wang, M. Shang, Y. Zhu, X. Xing, and P. Dang, "Jun Lin Small Stokes Shift and Two-Site Occupation in the ANb<sub>2</sub>O<sub>6</sub>: Cr<sup>3+</sup> (A = Zn/Mg) Phosphors Toward Highly Efficient Ultra-Broadband Near-Infrared Emission for Multifunctional Applications," *Advanced Optical Materials*, 12, https://doi.org/10.1002/adom.202302611.
- [42] M. Cannas, L. Vaccaro, and B. Boizot, "Spectroscopic Parameters Related to Non-Bridging Oxygen Hole Centers in Amorphous-SiO<sub>2</sub>," *Journal of Non-crystalline Solids* 352, no. 3 (2006): 203–208, https://doi.org/10.1016/j.jnoncrysol.2005.12.001.

[43] A. Kormányos, A. Thomas, M. N. Huda, et al., "Solution Combustion Synthesis, Characterization, and Photoelectrochemistry of CuNb<sub>2</sub>O<sub>6</sub> and ZnNb<sub>2</sub>O<sub>6</sub> Nanoparticles," *Journal of Physical Chemistry C* 120, no. 29 (2016): 16024–16034, https://doi.org/10.1021/acs.jpcc.5b12738.

- [44] F. Gu, S. F. Wang, M. K. Lü, et al., "Combustion Synthesis and Luminescence Properties of Dy<sup>3+</sup>-Doped MgO Nanocrystals," *Journal of Crystal Growth* 260, no. 3-4 (2004): 507–510, https://doi.org/10.1016/j.jcrysgro.2003.08.044.
- [45] P. Rajput, P. Vashishtha, G. Gupta, P. Singh, and K. Pathania, "Synthesis, Characterization and Photoluminescence of Dy<sup>3+</sup>-Doped MgZnO Nanophosphors," *Applied Physics A* 126, no. 8 (2020): 593, https://doi.org/10.1007/s00339-020-03783-0.
- [46] A. A. Khatun, T. Takei, M. D. Permana, N. Saito, and N. Kumada, "Synthesis and Characterization of Columbite Type Solid Solution Structured Niobate Mg<sub>1-x</sub>Ca<sub>x</sub>Nb<sub>2</sub>O<sub>6</sub>," *Journal of the Ceramic Society of Japan* 131, no. 8 (2023): 355–362DOI, https://doi.org/10.2109/jcersj2.23026.
- [47] G. El Fidha, N. Bitri, F. Chaabouni, et al., "Physical and Photocatalytic Properties of Sprayed Dy Doped ZnO Thin Films Under Sunlight Irradiation for Degrading Methylene Blue," RSC Advances 11, no. 40 (2021): 24917–24925, https://doi.org/10.1039/d1ra03967a.
- [48] T. S. Nwe, L. Sikong, R. Kokoo, and M. Khangkhamano, "Photocatalytic Activity Enhancement of Dy-Doped TiO<sub>2</sub> Nanoparticles Hybrid With TiO<sub>2</sub> (B) Nanobelts under UV and Fluorescence Irradiation," *Current Applied Physics* 20, no. 2 (2020): 249–254, https://doi.org/10.1016/j.cap.2019.11.008.
- [49] O. Yayapao, T. Thongtem, A. Phuruangrat, and S. Thongtem, "Sonochemical Synthesis of Dy-Doped ZnO Nanostructures and Their Photocatalytic Properties," *Journal of Alloys and Compounds* 576 (2013): 72–79, https://doi.org/10.1016/j.jallcom.2013.04.133.
- [50] N. Basavaraju, S. C. Prashantha, B. S. Surendra, et al., "Structural and Optical Properties of MgNb<sub>2</sub>O<sub>6</sub> NPs: Its Potential Application in Photocatalytic and Pharmaceutical Industries as Sensor," *Environmental Nanotechnology, Monitoring & Management* 16 (2021): 100581, https://doi.org/ 10.1016/j.enmm.2021.100581.
- [51] P. Muhambihai, V. Rama, and P. Subramaniam, "Photocatalytic Degradation of Aniline Blue, Brilliant Green and Direct Red 80 Using NiO/CuO, CuO/ZnO and ZnO/NiO Nanocomposites," *Environmental Nanotechnology, Monitoring & Management* 14 (2020): 100360–101532, https://doi.org/10.1016/j.enmm.2020.100360.
- [52] D. A. Raghupathy, G. Ramgopal, and C. R. Ravikumar, "Photocatalytic Degradation of Direct Green & Fast Orange Red Dyes: Electrochemical Sensor of Lead Using Cupric Oxide Nanoparticles Synthesized Via Sonochemical Route," Sensors International 3 (2022): 100204, https://doi.org/ 10.1016/j.sintl.2022.100204.
- [53] N. V. Mdlovu, K.-S. Lin, C.-J. Chang, Y.-S. Lin, and S. F. Hassan, "Adsorption and Photocatalytic Degradation of Dye Contaminants in Wastewater over W-Doped Titania Nanotubes," *Journal of the Taiwan Institute of Chemical Engineers* 146 (2023): 104863, https://doi.org/ 10.1016/j.jtice.2023.104863.
- [54] H. S. Yogananda, C. R. Ravikumar, S. R. Yashodha, and N. Dhananjaya, "Electrochemical Performance and Photocatalytic Activity of LaOCl: Eu3+: Its Application in Tin Sensing and Dye Degradation," *Materials Research In*novations (Taylor & Francis, 2024).
- [55] B. Abebe, C. R. Ravikumar, E. A. Zereffa, A. Naveen Kumar, and H. C. A. Murthy, "Photocatalytic and Superior Ascorbic

- Acid Sensor Activities of PVA/Zn-Fe-Mn Ternary Oxide Nanocomposite," *Inorganic Chemistry Communications* 123 (2021): 108343, https://doi.org/10.1016/j.inoche.2020.108343.
- [56] C. R. Ravikumar, P. Kotteeswaran, V. B. Raju, et al., "Influence of Zinc Additive and pH on the Electrochemical Activities of β-Nickel Hydroxide Materials and Its Applications in Secondary Batteries," *Journal of Energy Storage* 9 (2017): 12–24, https://doi.org/10.1016/j.est.2016.11.001.
- [57] K. Rudresha, A. Z. Hussain, C. R. Ravikumar, et al., "Structural, Electrochemical Sensor and Photocatalytic Activity of Combustion Synthesized of Novel ZnO Doped CuO NPs," *Materials Research Express* 10, no. 7 (2023): 075005, https://doi.org/10.1088/2053-1591/ace879.
- [58] V. Talapatadur, S. S. Hegde, N. Basavaraju, and K. Ramesh, "Solvothermal Method Synthesized SnS Nanoplates Composites for Electrochemical Sensing of Toxic Ions Hg<sup>2+</sup> and Pb<sup>2+</sup>," *Journal of the Iranian Chemical Society* 22, no. 1 (2025): 231–242, https://doi.org/10.1007/s13738-024-03145-0.